Principal Component Analysis for Estimating Population Density from Chord-Length Density

Martha A. Grover, Stephanie C. Barthe, and Ronald W. Rousseau
School of Chemical and Biomolecular Engineering, Georgia Institute of Technology, Atlanta, GA 30332

DOI 10.1002/aic.11866
Published online July 16, 2009 in Wiley InterScience (www.interscience.wiley.com).

The relationship between crystal population density and chord-length density (CLD) is complicated and depends on the size and shape of the crystals. Although estimation of chord-length density from the population density is relatively straightforward, the inversion of this procedure is problematic because the problem may be ill-conditioned for nonspherical particles. The focus of this work is on this inversion process. Since the relationship is a function of the crystal geometry, this manuscript considers various nonspherical shapes, including highly challenging needles. We describe an efficient method to estimate the population density from a measured CLD, to analyze the inversion process, and to quantify its limits. Since noise is present in the actual Focused Beam Reflectance Measurements, the case of restoration of the population density from noisy CLDs also is demonstrated. © 2009 American Institute of Chemical Engineers *AIChE J,* 55: 2260–2270, 2009

Keywords: crystallization, on-line monitoring, FBRM, population density, crystal shape

Introduction

Batch crystallization is widely used in the production of high-value added species, especially in the pharmaceutical and specialty chemical industries. It is commonly recognized that product properties and downstream processes are influenced by crystal morphology and size distribution. The ability to observe the evolution of the population density on-line and in real time would constitute a major asset in understanding and controlling crystallizer operation as well as the phenomena that influence product quality. This can be achieved through an accurate estimation of the population density. In this manuscript, we examine how measurements from an instrument that has gained significant use can be converted to population density.

Focused Beam Reflectance Measurements (FBRM) is among the Process Analytical Technologies (PAT) that hold promise for enhanced monitoring of crystallization. The technique is based on scattering of laser light and provides a methodology for on-line monitoring of the crystal population in either batch or continuous crystallization systems. The FBRM enables on-line determination of the chord-length density (CLD), which is a function of crystal size and shape and is related to the population density. However, inaccuracies in this CLD measurement have also been documented. A lack of contrast between the refractive indices of the solution and crystal could lead to a ''splitting'' of the chord, and the depth of focus of the FBRM must be properly set.[1] The effect of particle concentration on the measured CLD has also been studied recently, with weighting factors proposed to correct the signal.[2] Overall, many applications of the instrument have not come to fruition because of a general inability to use the measurements directly to quantify crystal size distributions by, for example, a population density function.

There have been several research groups that have made progress in dealing with this problem. Several publications analyze the relationship between population and chord-length densities and the recovery of the population density from the CLD.[1–10] In all of these, crystal shape is a major factor influencing the relationship. For example, Li and Wilkinson[3] developed a model based on a 2-D elliptical representation of the crystal and used an iterative nonnegative least-squares

Correspondence concerning this article should be addressed to M. A. Grover at martha.grover@chbe.gatech.edu

method to estimate the size distribution.[4] Wynn[8] used a method that can present difficulties with instability and is also based on a 2-D silhouette of the particles. Mazzotti and coworkers[5] used a 3-D representation of the particle and defined a relationship between CLD and population density that goes through the computation of a conversion matrix. Constraints were also implemented to enable the estimation of population density and were found necessary to overcome the issue of ill-conditioning of the matrix that prevented the pure inversion of the matrix.[5–7] More recently, 3-D optical modeling of crystals has been employed within the Monte Carlo simulation framework, and has provided a new explanation for the overestimation of small particles seen previously.[10]

A goal of this work is to develop a new, accurate, and constraint-free methodology for estimation of the population density from CLD measurements for various crystal shapes. The results are expected to lead to a better understanding of the fundamental limits inherent to the restoration of the population density for a nonspherical crystalline population, and to provide an analysis tool for determining the best settings on the FBRM. To demonstrate this methodology we compute the conversion matrix based on Monte Carlo sampling of random crystal orientations. This matrix is a function of the crystal geometry.[1] This step is similar to the approach proposed by Mazzotti and coworkers[5] based on 2-D projections of a 3-D crystal, although our inversion approach will also be applicable to conversion matrices computed using other optical models and assumptions. Unfortunately, the inversion problem—for example, computation of population density from the measured CLD—tends to be ill-conditioned, and constraints on the restored population density must be imposed to obtain a unique solution for the population density. Many of the constraints used by Mazzotti and workers[5,6] have a physical basis: for example, non-negativity and normalization of the densities. However, additional constraints may still be needed. Approaches employed include regularization to enforce smoothness of the solution, and upper bounds on the residual between the measured CLD and the model-predicted value.[5–7] Such constraints enable the computation of a unique solution. However, it is not clear that this unique solution for the population density is accurate. For example, some features of the population density might be overlooked due to the smoothness constraint imposed through regularization. In a previous study, we used this approach to estimate the population density from a measured CLD for paracetamol crystallized from an ethanol solution.[1] Good agreement was shown in comparing estimates recovered from FBRM measurements with those from ex situ sieving measurements.

The existing approaches for the inversion do not give a full understanding of which features in the population density can be accurately estimated. Moreover, the limits and robustness of both the measurement and the inversion are not well-understood or documented, and as a result there has been little industrial implementation of the direct inversion method. In this manuscript, a comprehensive comparison of the inversion process is given for octahedral crystals, elongated slabs, and needles. For each shape, several cases involving different types of population density functions (gamma, exponential, and bimodal) are analyzed. The influence of noise on the restoration process is examined, as well as the performance of the method compared with the Constrained Least Square Method (CLSM).

The method proposed in this work is based on a principal component analysis and the spectral method that is used to generate a basis for the population density; the basis elements are then divided into observable and unobservable subspaces. Population densities lying only in the observable subspace can be accurately reconstructed, whereas those lying in the unobservable subspace cannot. Additionally, we note that a combined approach is also possible for the inversion in which regularization and other constraints can be applied, as suggested by Mazzotti and coworkers.[5–7]

Methodology

Suppose that a population of crystals is divided according to size among N_b bins. Then for bin i, the largest crystal characteristic size is L_{i+1}, the smallest is L_i, the geometric mean is $\overline{L}_i$, and there are $\Delta N(\overline{L}_i)$ crystals in the bin. The length-weighted population density $\boldsymbol{n}_1$ is then given by

$$\boldsymbol{n}_1(\bar{L}_i) = \frac{\Delta \boldsymbol{N}(\bar{L}_i)\,\bar{L}_i}{(L_{i+1}-L_i)\left(\sum_{j=1}^{N_b}\Delta \boldsymbol{N}(\bar{L}_j)\;\bar{L}_j\right)}, \quad i = 1,\ldots N_b \tag{1}$$

where

$$\overline{L}_i = \sqrt{L_i L_{i+1}} \tag{2}$$

The chord-length density is obtained from the normalized chord-length histogram (chord counts in each bin) that is referred to as $\boldsymbol{k}(\overline{s}_i)$, where $\overline{s}_i$ is the mean chord length of the ith bin. The discretized normalized chord-length density can then be computed as

$$\boldsymbol{q}(\overline{s}_i) = \frac{\boldsymbol{k}(\overline{s}_i)}{(s_{i+1}-s_i)\left(\sum_{j=1}^{N_b}\boldsymbol{k}(\overline{s}_j)\right)} \tag{3}$$

where

$$\overline{s}_i = \sqrt{s_i s_{i+1}} \tag{4}$$

The relationship between the length-weighted population density $\boldsymbol{n}_1$ and the chord-length histogram $\boldsymbol{k}$ is defined by

$$\boldsymbol{k} = \Psi \boldsymbol{n_1} \tag{5}$$

where Ψ is a square conversion matrix relating the histogram $\boldsymbol{k}$ and the density $\boldsymbol{n}_1$. The length-weighting of the population size is required since large crystals are sampled with a higher probability.[5] The matrix Ψ is computed using Monte Carlo simulations and strongly depends on the geometry of the crystals.[3,4,11]

As part of our inversion process, we apply the spectral method, which can only be applied to symmetric matrices. Therefore, both sides of Eq. 5 are multiplied by Ψ^T, where the matrix $\Psi^T\Psi$ is symmetric:

$$\Psi^T \boldsymbol{k} = \Psi^T \Psi \boldsymbol{n_1} \tag{6}$$

Defining

$$\boldsymbol{A} = \Psi^{\mathbf{T}}\Psi \tag{7}$$

and

$$\boldsymbol{b} = \Psi^{\mathbf{T}}\boldsymbol{k} \tag{8}$$

Equation 6 becomes

$$\boldsymbol{b} = \boldsymbol{A}\boldsymbol{n_1} \tag{9}$$

where $\boldsymbol{A}$ is a real symmetric matrix and $\boldsymbol{b}$ is a real vector.

The goal here is to determine when the population density $\boldsymbol{n}_1$ can be accurately estimated. Therefore, the measurement of the chord-length histogram $\boldsymbol{k}$ will be used as a starting point, and the spectral method will be used to estimate the population density. A basis $\boldsymbol{U}$ can be computed by a singular value decomposition of Ψ, or equivalently by computing the eigenvectors $\boldsymbol{u}_i$ of matrix $\boldsymbol{A}$. An advantage of computing this orthonormal basis is that the inversion of the relationship in Eq. 5 can be accomplished using scalar computations only, without requiring a matrix inversion. In the new coordinate system defined by this basis, some coordinates may be ill-conditioned, which will be indicated by their near-zero singular values. We refer to these coordinates as "unobservable" in the FBRM measurement. This approach allows us to analyze the inversion process and to compute reconstructions of $\boldsymbol{n}_1$ in the observable subspace. The accuracy of the recovery and the sensitivity to noise are also investigated and quantified.

Spectral method

Assume that $\boldsymbol{A}$ is a real symmetric matrix and its eigenvalues $\lambda_i = {\sigma_i}^2$ and eigenvectors $\boldsymbol{u}_i$ have been computed. The σ_i are thus defined to be the singular values of the matrix Ψ. An orthonormal basis $\boldsymbol{U}$ can be defined using the eigenvectors.[12] We use a principal component analysis to invert the relationship given by Eq. 9. This procedure is well known and a thorough description can be found elsewhere[13–16]; a brief summary of the method is available in Appendix A.

Equation 9 can be solved for $\boldsymbol{n}_1$ as

$$\boldsymbol{n}_1 = \sum_{i=1}^{m} \left(\frac{(\boldsymbol{u_i} \cdot \boldsymbol{b})}{\sigma_i^2} \right) \boldsymbol{u_i} \tag{10}$$

We use Eq. 10 to compute $\boldsymbol{n}_1$ from the chord-length histogram $\boldsymbol{k}$, which is the foundation for our estimation of population densities from chord-length measurements. Considering that ${\sigma_i}^2$ is the denominator in Eq. 10, this method can only be applied if all singular values are nonzero. However, any eigenvectors that have zero singular values should not be inverted anyway, since they represent features in $\boldsymbol{n}_1$ that have no influence on $\boldsymbol{k}$. The eigenvectors are thus divided into two subsets and corresponding subspaces: an observable set that corresponds to nonzero eigenvalues, and an unobservable set corresponding to zero eigenvalues. Eigenvalues that are approximately zero correspond to ill-conditioned coordinates, and they are also included in the unobservable subspace. They represent features in $\boldsymbol{n}_1$ that have a negligible effect on $\boldsymbol{k}$, and thus would be masked by even a slight amount of measurement noise. Determining the cutoff value m' to delineate those subspaces is not straightforward. Several studies have been published comparing various methodologies for cutoff selection in principal component analysis.[13,16] According to the work of Jackson,[13] the "Broken Stick" methodology gives an estimation of the cutoff value, nonetheless the SCREE and the PRESS methods remain widely used.[14,15] However, the broken stick method is intended for finding random patterns in data matrices, whereas this manuscript focuses on the inversion of a matrix equation with measurement noise. The inversion problem is conceptually different since small singular values may be important for accurate inversion. For the noise-free case, our cutoff is determined by trial and error, similar to the SCREE method. Since our eigenvalue spectra do not exhibit clear break points, the PRESS method is less appropriate. A recent study on the estimation of size distribution does not use any rigorous criterion for the cutoff,[17] and the selection is similar to the PRESS idea. In this article, we present a criterion for determining the cutoff in the presence of measurement noise. This criterion might also be useful in other inversion applications with noise.

We arrange the singular values σ_i of Ψ in descending order, with m' defined to delineate the two subspaces. Thus:

$$\boldsymbol{n}_{1,\mathrm{obs}} = \sum_{i=1}^{m'} \alpha_i \boldsymbol{u_i} \tag{11}$$

$$\boldsymbol{n}_{1,\mathrm{unobs}} = \sum_{i=m'+1}^{m} \alpha_i \boldsymbol{u_i} \tag{12}$$

Only the observable portion of $\boldsymbol{n}_1$ can be estimated from $\boldsymbol{k}$, so Eq. 10 is replaced with the modified version:

$$\boldsymbol{n}_{1,\mathrm{est}} = \sum_{i=1}^{m'} \left(\frac{(\boldsymbol{u_i} \cdot \boldsymbol{b})}{\sigma_i^2} \right) \boldsymbol{u_i} \tag{13}$$

In the absence of noise in the chord-length measurement, $\boldsymbol{n}_{1,\mathrm{obs}} = \boldsymbol{n}_{1,\mathrm{est}}$. Ideally, $\boldsymbol{n}_{1,\mathrm{obs}} \cong \boldsymbol{n}_1$ and $\boldsymbol{n}_{1,\mathrm{unobs}} \cong \boldsymbol{0}$, but if this is not the case, then an accurate estimate of $\boldsymbol{n}_1$ cannot be obtained from the FBRM measurements, at least not without additional information on the characteristics of $\boldsymbol{n}_1$.

The spectral method can be used to analyze the estimation process for a prespecified population density $\boldsymbol{n}_1$ (Analysis), or it can be used to estimate an unknown $\boldsymbol{n}_1$ from FBRM measurements (Estimation). In practice, the analysis should be performed for expected values of $\boldsymbol{n}_1$, before the use of the method to estimate the unknown $\boldsymbol{n}_1$. In either situation, the cutoff m' must be determined. To select m' we first define the error caused by neglecting a portion of the eigenvalues:

$$\boldsymbol{e} = \boldsymbol{n}_1 - \boldsymbol{n}_{1,\mathrm{est}} = \left(\sum_{i=1}^{m} \frac{\boldsymbol{u}_i \cdot \boldsymbol{b}}{\sigma_i^2} \boldsymbol{u}_i - \sum_{i=1}^{m'} \frac{\boldsymbol{u}_i \cdot \tilde{\boldsymbol{b}}}{\sigma_i^2} \boldsymbol{u}_i \right) \tag{14}$$

where $\tilde{\boldsymbol{b}} = \Psi^{\mathbf{T}}(\boldsymbol{k} + \boldsymbol{v})$, and $\boldsymbol{v}$ is a noise vector. Canceling terms and rearranging yields

$$\boldsymbol{e} = \sum_{i=m'+1}^{m} \frac{\boldsymbol{u}_i \cdot \left(\Psi^{\mathrm{T}} \boldsymbol{k}\right)}{\sigma_i^2} \boldsymbol{u}_i - \sum_{i=1}^{m'} \frac{\boldsymbol{u}_i \cdot \left(\Psi^{\mathrm{T}} \boldsymbol{v}\right)}{\sigma_i^2} \boldsymbol{u}_i \tag{15}$$

We define $\boldsymbol{e}_1$ as the error due to the truncation, and $\boldsymbol{e}_2$ as the error due to noise in the measurement:

$$\boldsymbol{e}_1 = \sum_{i=m'+1}^{m} \frac{\boldsymbol{u}_i \cdot \left(\Psi^{\mathrm{T}} \boldsymbol{k}\right)}{\sigma_i^2} \boldsymbol{u}_i = \sum_{i=m'+1}^{m} \frac{(\Psi \boldsymbol{u}_i) \cdot \boldsymbol{k}}{\sigma_i^2} \boldsymbol{u}_i \tag{16}$$

$$\boldsymbol{e}_2 = -\sum_{i=1}^{m'} \frac{\boldsymbol{u}_i \cdot \left(\Psi^{\mathrm{T}} \boldsymbol{v}\right)}{\sigma_i^2} \boldsymbol{u}_i = -\sum_{i=1}^{m'} \frac{(\Psi \boldsymbol{u}_i) \cdot \boldsymbol{v}}{\sigma_i^2} \boldsymbol{u}_i \tag{17}$$

Ideally, we would like each of these errors to be as close to zero as possible. However, there is a tradeoff, since when $\boldsymbol{v}$ is nonzero, the truncation error in Eq. 16 goes to zero as m' approaches m, whereas the noise-generated error in Eq. 17 goes to zero as m' goes to 0.

We set our desired accuracy on the inversion using

$$e_{\mathrm{rel}} = \sqrt{\frac{\boldsymbol{e} \cdot \boldsymbol{e}}{\boldsymbol{n}_1 \cdot \boldsymbol{n}_1}} = \sqrt{\frac{\boldsymbol{e}_1 \cdot \boldsymbol{e}_1 + \boldsymbol{e}_2 \cdot \boldsymbol{e}_2}{\boldsymbol{n}_1 \cdot \boldsymbol{n}_1}} < \varepsilon_{\mathrm{tol}} \tag{18}$$

In the first part of the results section, we assume that there is no noise such that $\boldsymbol{v} = 0$ and $\boldsymbol{e} = \boldsymbol{e}_1$. The cutoff m' is determined such that $\varepsilon_{\mathrm{tol}} < 1\%$. In the second part, we consider the presence of noise and the value of m' can be made smaller to address the tradeoff between minimizing $\boldsymbol{e}_1$ and $\boldsymbol{e}_2$. It is interesting to note that $\boldsymbol{e}_2$ is only a function of $\boldsymbol{v}$, and not of $\boldsymbol{k}$ or $\boldsymbol{n}_1$. To quantify the size and importance of $\boldsymbol{e}_2$, we use the two-norm based on the vector dot product:

$$\left\|\boldsymbol{e}_2\right\|_2^2 = \boldsymbol{e}_2 \cdot \boldsymbol{e}_2 = \sum_{i=1}^{m'} \frac{\left(\boldsymbol{u}_i \cdot \left(\Psi^{\mathrm{T}} \boldsymbol{v}\right)\right)^2}{\sigma_i^4} = \sum_{i=1}^{m'} \frac{((\Psi \boldsymbol{u}_i) \cdot \boldsymbol{v})^2}{\sigma_i^4} \tag{19}$$

Here, as in Eq. 18, we have used the fact that the eigenvectors are orthonormal. Hence we can derive the following inequality using the definition of the vector dot product:

$$\begin{aligned} ||\boldsymbol{e}_2||_2^2 &= \sum_{i=1}^{m'} \frac{1}{\sigma_i^4} ||(\Psi \boldsymbol{u}_i) \cdot \boldsymbol{v}||_2^2 \leq \left(\sum_{i=1}^{m'} \frac{1}{\sigma_i^4} ||(\Psi \boldsymbol{u}_i)||_2^2 \right) ||\mathbf{v}||_2^2 \\ &= C(m')^2 ||\mathbf{v}||_2^2 = UB(m')^2 \end{aligned} \tag{20}$$

Here. we have defined UB as the upper bound on $\|\boldsymbol{e}_2\|_2$, and C as the proportionality constant in this upper bound. The purpose for deriving this bound is to be able to verify that $\|\boldsymbol{e}_2\|_2 \leq \|\boldsymbol{e}_1\|_2$. This ensures that the noise does not dominate the error. If necessary, the cutoff m' can be adjusted to smaller values so that the inequality in Eq. 20 can be satisfied, although in that case it will not be possible to keep $e_{\mathrm{rel}} \leq \varepsilon_{\mathrm{tol}}$ in Eq. 18.

An alternative criterion for selecting m' could be to minimize $\|\boldsymbol{e}\|_2$, by averaging over a large number of realizations of the noise vector. However, this would tend to increase m' even further when the estimated noise level is low, which could reduce the robustness of the inversion if higher than expected noise levels are encountered in practice.

We first present the steps required for analysis of a known population distribution.

Analysis.

(1) Determine the shape of the crystals, the accuracy $\varepsilon_{\mathrm{tol}}$ required in the estimated $\boldsymbol{n}_1$, and the standard deviation ω of the zero-mean measurement noise for each bin in $\boldsymbol{k}$. In general the noise level will not be known exactly, but it can be estimated from repeated experiments, steady-state experiments, or even a stochastic model of the crystallization process.

(2) Compute the conversion matrix Ψ for the desired shape and then the corresponding symmetric matrix $\boldsymbol{A}$, as defined by Eq. 7.

(3) Compute the eigenvalues and eigenvectors of $\boldsymbol{A}$ and Ψ. Plot the corresponding singular values σ_i. Determine the maximum cutoff value $m'_{\max}$ such that $\sigma_i > 0$.

(4) Considering first the noise-free case, determine the cutoff $m' \leq m'_{\max}$ to achieve $\varepsilon_{\mathrm{tol}}$ in $\boldsymbol{n}_1$ in Eq. 18. m' should be as small as possible while still achieving $e_{\mathrm{rel}} < \varepsilon_{\mathrm{tol}}$, since small σ_i will tend to amplify measurement noise in $\boldsymbol{k}$ during the inversion process.

(5) Using Eq. 20, compute the upper bound on $\|\boldsymbol{e}_2\|_2$ in the presence of measurement noise. If $UB(m')$ is greater than the value of $\|\boldsymbol{e}_1\|_2$ computed using Eq. 16, then m' could be adjusted to smaller values until the two error predictions are of the same size. Because the upper bound may overpredict the effect of the noise, only a range of the possible m' can be established, between the value from Step 5 up to the value from Step 4.

When the goal is to estimate an unknown $\boldsymbol{n}_1$ from a measured noisy $\boldsymbol{k}$, the following procedure can be used:

Estimation.

(1) Determine the shape of the crystals, the accuracy $\varepsilon_{\mathrm{tol}}$ desired in the estimated $\boldsymbol{n}_1$, and the standard deviation vector ω of the zero-mean measurement noise for each bin in $\boldsymbol{k}$.

(2) Compute the conversion matrix Ψ for the desired shape, and then the corresponding symmetric matrix $\boldsymbol{A}$ as defined by Eq. 7.

(3) Compute the eigenvalues and eigenvectors of $\boldsymbol{A}$. Plot the singular values $\sigma_i = \lambda_i^{1/2}$. Determine the maximum cutoff value $m'_{\max}$ such that $\sigma_i > 0$.

(4) Select $m' \leq m'_{\max}$ based on the FBRM noise level, using $\|\boldsymbol{e}_2\|_2^2 \leq \varepsilon_{\mathrm{tol}}$. This criterion is used to set m' so that the effect of measurement noise of $\boldsymbol{n}_1$ does not exceed $\varepsilon_{\mathrm{tol}}$. Note that this does not guarantee a good reconstruction of the unknown $\boldsymbol{n}_1$.

There is no guarantee on the accuracy of the reconstruction in the observable subspace, since $\boldsymbol{n}_1 = \boldsymbol{n}_{1,\mathrm{obs}} + \boldsymbol{n}_{1,\mathrm{unobs}}$, and $\boldsymbol{n}_{1,\mathrm{unobs}}$ cannot be recovered by definition since $\boldsymbol{k}$ is not sensitive to this portion of $\boldsymbol{n}_1$. If $\boldsymbol{n}_{1,\mathrm{unobs}}$ is not approximately zero, then there will be significant error in the reconstruction. This is why it is important to perform the analysis procedure for typical expected $\boldsymbol{n}_1$ vectors, and to examine the singular value spectrum. In the Results and Discussion section, we observe that the basis vectors for large values of m' tend to be highly oscillatory and may not be needed to reconstruct typical $\boldsymbol{n}_1$ distributions. To summarize, it is clearly not possible to reconstruct every possible $\boldsymbol{n}_1$ vector for a conversion matrix that is not full rank. However, we show that for many population densities of practical interest in crystallization, accurate estimation should be possible as long as the noise level is not too high.

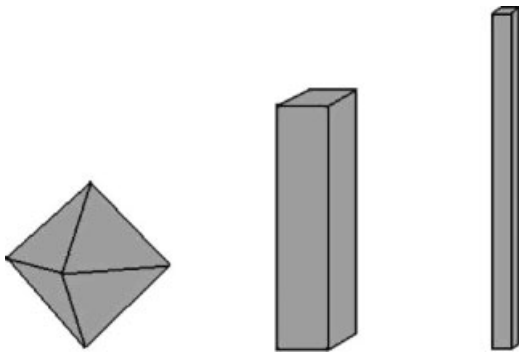

Figure 1. Crystal shapes studied: octahedral, slab (aspect ratio 1:1:5) and needle (aspect ratio 1:1:20).

Results and Discussion

Our method for inversion is tested on several realistic examples to evaluate the accuracy of the estimated $\boldsymbol{n}_1$; three crystal morphologies and three distributions representing typical crystallization operations are investigated. Since the relationship defined by Eq. 5 is a function of the shape of the crystals, we consider the three nonspherical shapes shown in Figure 1 as being representative of broad classes of crystal categories: bulky, elongated, and needle-like. To characterize the size L of each crystal, we use the equivalent spherical diameter, based on the volume of the crystal.

The conversion matrix Ψ was computed for each of the three geometries considered using 10,000 realizations for each of the 90 crystal sizes. The corresponding matrix $\boldsymbol{A}$ was computed according to Eq. 7. $\boldsymbol{A}$ is a real symmetric 90×90 conversion matrix ($m = 90$), since our FBRM is set to classify the chord length in 90 channels or bins. The bins are defined by the log scale used by the FBRM, and they are the same for both $\boldsymbol{k}$ and $\boldsymbol{n}_1$. Since Ψ depends on the crystal shape, $\boldsymbol{A}$ is also different for each shape. First, we determine which eigenvectors in the basis have an influence on the chord-length histogram. The singular values of the matrix Ψ are computed for each of the three geometries, and are plotted in Figure 2.

For the octahedral crystals, the nonzero singular values (solid curve) span four orders of magnitude. The challenge is to determine a value of m' that enables accurate estimation, especially in the presence of noise. In Appendix A, one can see that features in $\boldsymbol{n}_1$ associated with singular values of $\sigma \gg 1$ will tend to be amplified in $\boldsymbol{k}$, whereas singular values of $\sigma \ll 1$ will attenuate the corresponding features in $\boldsymbol{k}$. For all three crystal shapes, this transition occurs around $m' = 25$.

The singular values of the slab-like geometry are shown by the dashed curve in Figure 2. Most of the singular values range over four orders of magnitude. However, a sharp drop-off exists in which the last five eigenvalues are extremely small. Therefore, the cutoff m' should not be set lower than 85 (or else the inversion may amplify noise by a factor of $\sim 10^9$). The needle-like geometry exhibits qualitative behavior that is similar to that of the slab. Most λ's extend over four orders of magnitude. The cutoff value m' is limited by the last 11 extremely small singular values (dashed-dot curve).

At this point, it appears that the slab and needle may be more difficult to invert than the octahedral, due to the existence of more singular values that are approximately zero. However, all three shapes have a large number of singular values that are greater than 10^{-1}, so if the original noise level in $\boldsymbol{k}$ is very low, then an amplification of 100 ($1/\sigma_i^2$) may still be acceptable.

To evaluate the inversion process, we must also consider the particular crystal size distribution. The population density distributions examined here were chosen because each represents a particular mode of crystallizer operation and resulting product size distribution that is:

- Gamma distribution—representative of crystals produced in batch crystallization
- Exponential distribution—representative of crystals produced in continuous crystallization in which anomalous growth, agglomeration, and breakage can be neglected
- Bimodal distribution—representative of complex batch crystallization in which seeding or other phenomena lead to the crystal size distribution having two modes.

We first discuss in detail the results of our analysis of systems in which the crystal population density follows a gamma distribution function. Using the outcome as a point of departure, we then contrast that behavior with results obtained from exponential and bimodal distribution functions. Finally, we impose noise on a hypothetical signal from an FBRM instrument to explore how the interpretation of that signal is affected by the noise.

Gamma distribution

Gamma distribution functions are defined by:

$$\boldsymbol{n}_1(\bar{L}_i) = \gamma\, \bar{L}_i^{\beta-1} \frac{e^{-\bar{L}_i/\theta}}{(\beta-1)!\theta^{\beta}} \tag{21}$$

where β is a shape factor, θ is a scale parameter and γ is a normalizing coefficient. In this work, the parameters are selected so that $L_{\text{mode}} = 400\ \mu\text{m}$ ($\beta = 9$ and $\theta = 50$).

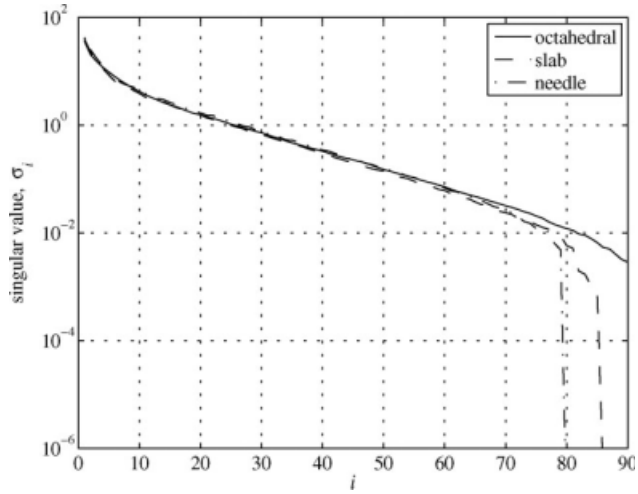

Figure 2. Singular values of Ψ for the octahedral, slab, and needle-like crystals.

Octahedral crystals. We first consider octahedral crystals whose length-weighted population density follows a gamma distribution in the limit of no FBRM noise. We follow the analysis procedure in the previous section and set $\varepsilon_{tol} = 0.01$, so that the reconstructed $\boldsymbol{n}_1$ will be accurate within 1%. Therefore, we compute that the cutoff value $m' = 13$, which leads to σ's ranging over one order of magnitude in the observable subspace. Figure 3 illustrates the projection of $\boldsymbol{n}_1$ in the observable subspace such that $\boldsymbol{n}_1 \cong \boldsymbol{n}_{1,obs}$. With only 13 eigenvectors, the projection onto the observable subspace is accurate to 1%. Having established the accuracy of the nominal projection, we now focus on the estimation of $\boldsymbol{n}_1$ from a measured chord-length histogram $\boldsymbol{k}$. Using the gamma distribution in Eqs. 21 and 5, we obtain the "measured" $\boldsymbol{k}$. Eq. 13 is then used to estimate $\boldsymbol{n}_1$. An accurate reconstruction of $\boldsymbol{n}_1$ is obtained, as both the initial density $\boldsymbol{n}_1$ (solid curve), the projected density $\boldsymbol{n}_{1,obs}$ (square symbols) and the reconstructed density $\boldsymbol{n}_{1,est}$ (cross symbols) are in agreement, as shown in Figure 3. As mentioned previously, in the noise-free limit, $\boldsymbol{n}_{1,obs} = \boldsymbol{n}_{1,est}$ by definition, which is confirmed by Figure 3. Figure 4 provides further confirmation of the successful inversion. The original chord-length histogram $\boldsymbol{k}$ (solid curve) coincides with the estimated population density $\boldsymbol{k}_{est} = \Psi\boldsymbol{n}_{1,est}$ (cross symbols). A slight waviness in $\boldsymbol{n}_{1,est}$ exists at the largest sizes, which causes the 1% error—using a value of $m' > 13$ would be required to reduce this error.

Slab-like crystals (Aspect ratio 1:1:5). We now consider slab-like crystals with the gamma distribution. As with the octahedral crystals, we set $\varepsilon_{tol} = 0.01$, which results in an eigenvalue cutoff of $m' = 7$. Thus, seven basis vectors will now be used, compared with 13 for the octahedral crystals. From Figure 2, we see that for the octahedral crystals, $\sigma_{m'}$ is smaller than for the slab. Thus, the inversion of the gamma distribution may now be slightly less noise-sensitive for the slab, compared with the octahedron. Similar agreement is achieved among the recovered $\boldsymbol{n}_{1,est}$ and the initial length-weighted population density $\boldsymbol{n}_1$, as in the octahedral case of Figure 3. Good agreement was also achieved in chord-length histogram, similar to that plotted in Figure 4 for the octahedral case. This case is not plotted but its performance is summarized in Table 1.

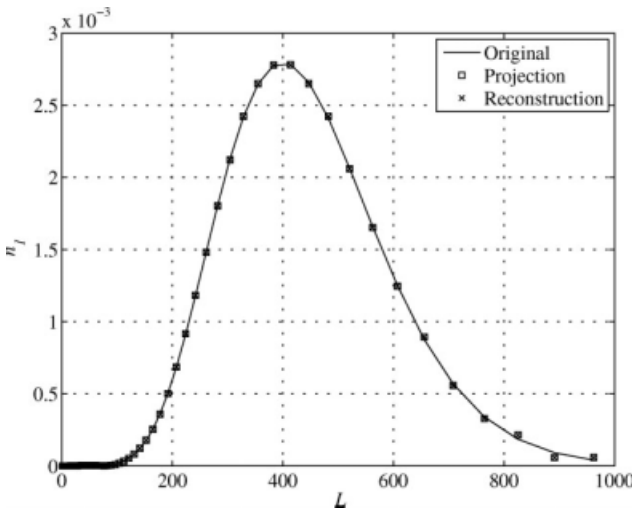

Figure 3. Projection of n_1 onto the observable and unobservable subspaces, and recovered population density through the spectral method for an octahedral shape, using $m' = 13$.

Similar plots are obtained for slab and needle-like crystals.

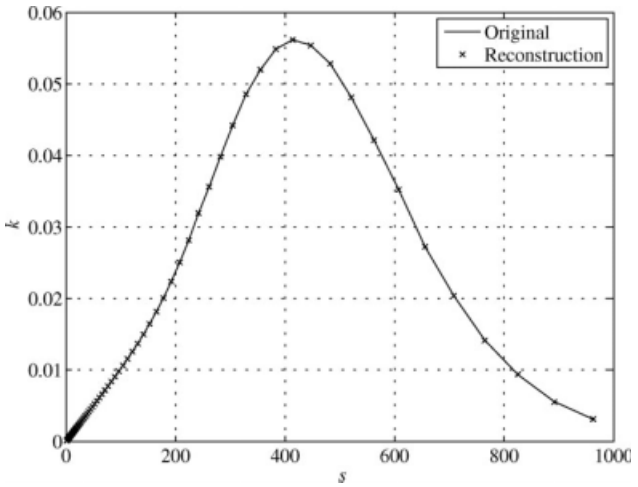

Figure 4. Chord length histogram k for the gamma distribution and an octahedral shape, using $m' = 13$.

The actual value is compared with the value computed using the reconstructed $\boldsymbol{n}_1$.

Needle-like crystals (Aspect ratio 1:1:20). For needle-like crystals, the cutoff is again determined by the 1% accuracy imposed on the reconstructed $\boldsymbol{n}_1$ by ε_{tol}, resulting in $m' = 7$. Thus, a similar number of eigenvectors is needed for the needle, compared with the slab, and the value of $\sigma_{m'}$ is also similar to the slab. Due to the similar characteristics of their singular value spectra, we expect similar inversion properties for the needle and slab, and this should be true with and without noise. The projections of $\boldsymbol{n}_1$ and their corresponding $\boldsymbol{k}$ all lead to good reconstructions, with results again similar to those pictured in Figures 3 and 4. The results for the gamma distribution for all three shapes are summarized in Table 1.

Exponential distribution

A key difference between exponential and gamma distributions is that the former has a larger number of small crystals. A nucleation event is indicated by an increase in the number of small crystals, which is a common disturbance in

Table 1. Summary of Reconstruction Error for the Three Crystal Shapes and the Three Distributions

		Gamma	Exponential	Bimodal
Octahedral	m'	13	87	36
	$\sigma_{max}/\sigma_{m'}$	12.4	7160	82.7
	e_{rel}	0.00754	0.00783	0.00854
Slab	m'	7	85	32
	$\sigma_{max}/\sigma_{m'}$	7.34	47600	70.3
	e_{rel}	0.00964	0.225	0.00933
Needle	m'	7	79	31
	$\sigma_{max}/\sigma_{m'}$	6.95	8750	61.2
	e_{rel}	0.00786	0.401	0.00788

crystallization, and, thus, it is important to be able to estimate accurately the population of small crystals.

Octahedral crystals. As with the gamma distribution, we specify $\varepsilon_{tol} = 0.01$. However, with the exponential distribution, an extremely high value of $m' = 87$ is required to achieve this level of accuracy. This comparison can be seen in Table 1. The singular values required for this value of $m' = 87$ now span over almost four orders of magnitude, which can be seen in Figure 2 and also in Table 1. Figure 5 illustrates the reconstruction of $\boldsymbol{n}_1$. The greatest errors in reconstruction are at the smallest sizes, suggesting that the reconstruction may be most challenging there.

Slab-like crystals (Aspect ratio 1:1:5). Figure 6 shows the exponential distribution for the slab-like crystals. Recall that the minimum value of m' is 85 for this crystal shape, due to the five near-zero eigenvalues in Figure 2. With this constraint, we are not able to achieve $\varepsilon_{tol} = 0.01$, and by setting $m' = 85$ we achieve an error of 22% ($e_{rel} = 0.22$). Figure 6 illustrates the resulting error when $\boldsymbol{n}_1$ is reconstructed using this subspace. In fact, the error is concentrated at the lowest sizes, and the reconstruction is quite accurate over the majority of the sizes. Note that the error defined by Eq. 21 does not take into account the width of each bin, and that the bins are logarithmically distributed such that the bins at the smallest sizes have the smallest width. This causes the small crystals to dominate our error calculation. In any case, we use this measure of error in part because it may be desirable to estimate these smallest bins accurately so as to monitor nucleation events. Of the eigenvectors that are retained for the observable space, the range of singular values is more than four orders of magnitude. These are easily invertible in the noise-free case considered here, and Figure 6 shows that $\boldsymbol{n}_1$ and $\boldsymbol{n}_{1,est}$ are virtually identical above 10 μm.

Needle-like crystals (Aspect ratio 1:1:20). The results for the needle-like crystals are similar to those of the slab. Due to the near-zero singular values, the minimum value of m' is 79, and this cutoff yields a projection error of 40%. Oscillations for the lower sizes are, as shown in Figure 7, even more noticeable due to the highly nonspherical shape of the crystals, and the accuracy of the restoration of the fines population (below 10 μm) is poor. However, the reconstruction for crystals larger than 10 μm is good.

Compared with the gamma distribution, the inversion of the exponential distribution is more challenging. Due to the large number of crystals at the smallest sizes, and the small bin sizes at the smallest crystal sizes, it is difficult to estimate the fines distribution accurately, particularly for the slab-like and needle-like crystals.

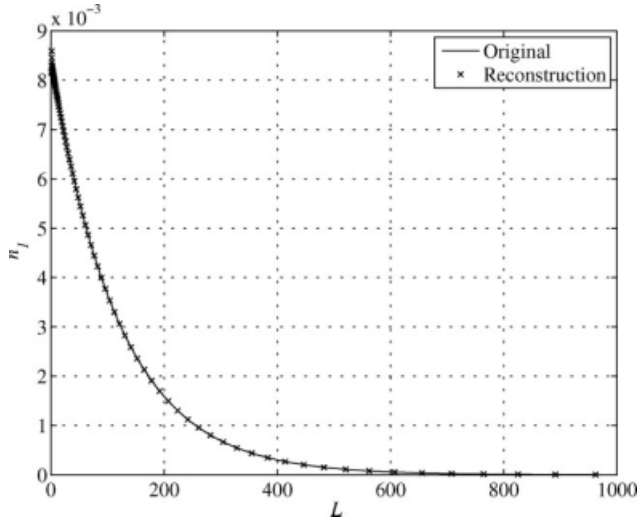

Figure 5. Reconstruction of n_1 from an exponential distribution for an octahedral shape, using $m' = 87$.

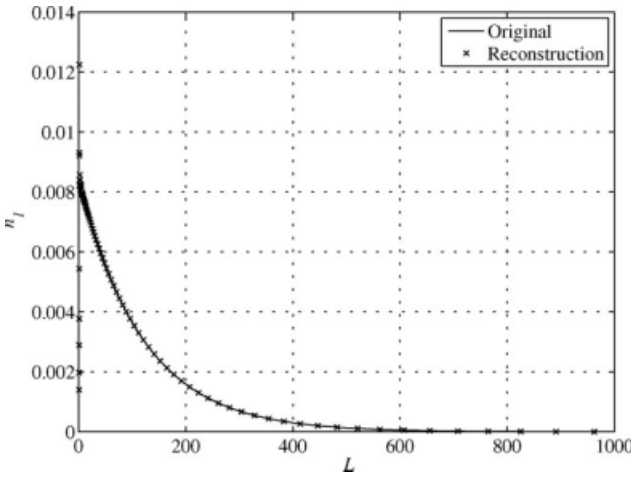

Figure 6. Reconstruction of n_1 from an exponential distribution for the slab shape, using $m' = 85$.

Bimodal distribution

Bimodal distributions can present significant challenges in analysis and modeling, and so we examine how our methodology handles such systems. The same crystal shapes are considered, and the same estimation procedure is employed. The bimodal distribution is constructed from two gamma distributions, and estimates are achieved at 1% error for all crystal shapes. Figure 8 shows the projection and reconstruction for the octahedral crystals, and good reconstruction is

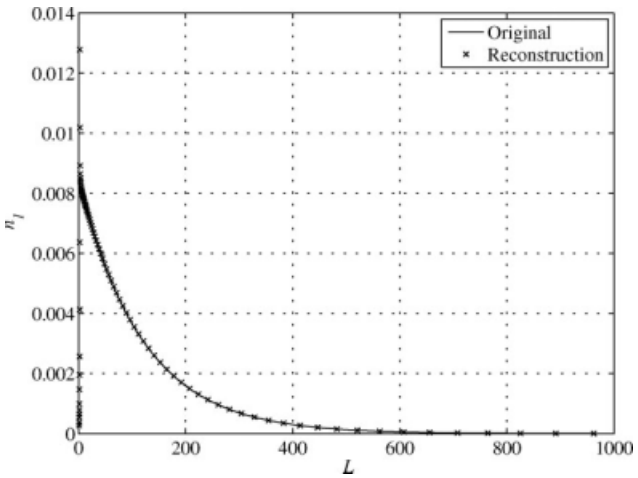

Figure 7. Reconstruction of n_1 from an exponential distribution for the needle shape, using $m' = 79$.

seen. Results similar to those with the gamma distribution are seen for the slab-like and needle-like crystals. The plots are not shown here, but the results are summarized in Table 1. Compared with the gamma distribution, more eigenvectors are required to achieve the 1% accuracy in the projection. The corresponding ranges of the singular value magnitudes in the observable subspace have increased by an order of magnitude (compared with gamma). These results indicate that the estimation of $\boldsymbol{n}_1$ in the observable subspace may be more difficult than for gamma, but should be less difficult than for the exponential distribution.

Influence of noise

In the noise-free case, the spectral method provides good estimates of $\boldsymbol{n}_1$ for the gamma and bimodal distributions for all three crystal shapes considered. When the exponential distribution is analyzed, the estimation is good except at the smallest crystal sizes, in which case the estimates are highly oscillatory around the actual mean. However, real CLD measurements are noisy, making estimation of the population density more difficult, and this will be especially true for the basis vectors with small singular values σ, due to the σ in the denominator of Eq. 17.

To investigate the role of noise, we measure the steady-state noise in each channel, using our FBRM measurements obtained for paracetamol crystallization from ethanol.[1] We estimate the standard deviation vector ω of the FBRM signal for each bin of the vector $\boldsymbol{k}$, and then add this zero-mean noise to the noise-free $\boldsymbol{k}$ computed for each of our three distributions. Because the experiments and associated noise are for octahedral crystals, we analyze that shape only. In general, the noise may also depend on the crystallization time and other details of the process, and our steady-state noise levels are only intended to explore the effect of noise in the FBRM measurements. The noise level also depends on the integration time of the FBRM measurement, and we consider measurement time increments of 10, 20, and 30 s. On increasing this time step increases the number of counts in each bin and therefore decreases the noise level.

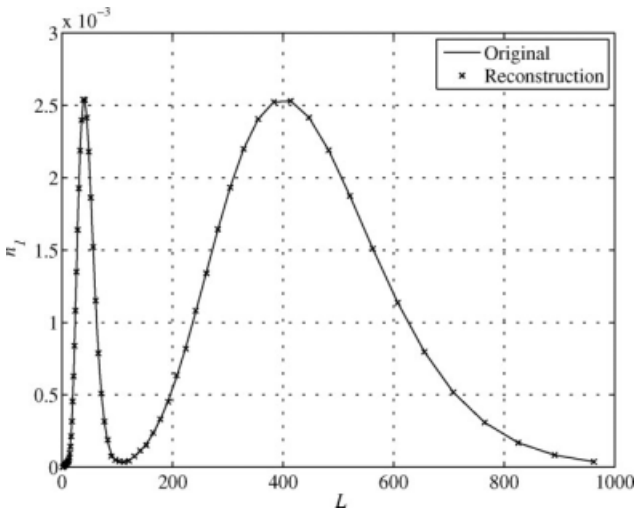

Figure 8. Reconstruction of n_1 from a bimodal distribution for the octahedral shape, using $m' = 36$.

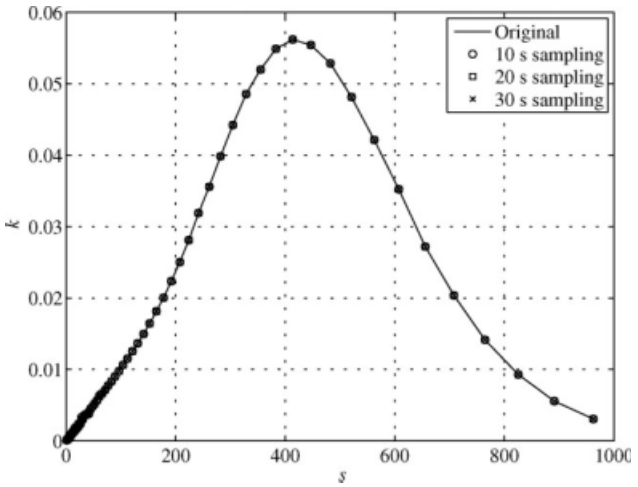

Figure 9. Addition of noise to the k computed for the gamma distribution.

The three different noise levels are associated with FBRM sampling at three different integration times.

To obtain insight on the influence of noise on the recovery process, the zero-mean Gaussian-distributed noise vector $\boldsymbol{v}$ is added to the initial $\boldsymbol{k}$ (Figure 9). The highest noise appears in the smallest bins, which further complicates the estimation of small crystals. The recovery of the population through the spectral method gives good results, shown in Figure 10. The estimated population density displays a very slight oscillation up to 100 μm for the sampling time of 10 s (circle symbols), and the estimation is improved when the sampling time is increased to 20 or 30 s. The results, averaged over 1000 realizations of the noise, are summarized in Table 2.

Note that the same value of $m' = 13$ from the noise-free study is used here for the gamma distribution. Earlier in the article, we suggested the guideline of $\|\boldsymbol{e}_2\|_2 \leq \|\boldsymbol{e}_1\|_2$ to ensure that the measurement noise does not dominate the

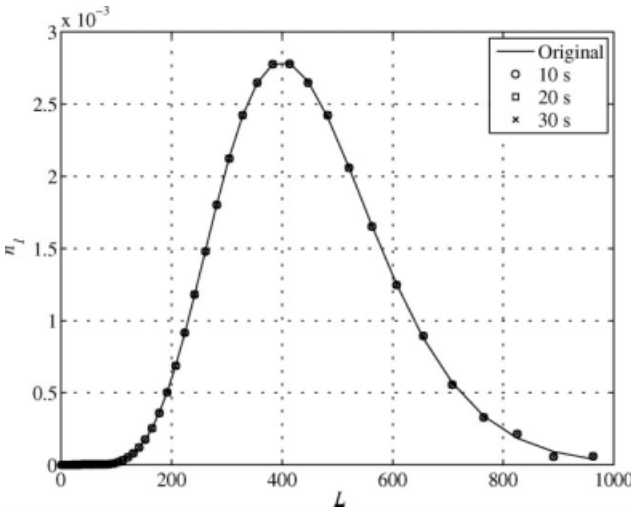

Figure 10. Reconstruction of the gamma population density from a noisy chord-length histogram, using $m' = 13$.

The crystal shape is octahedral.

Table 2. Estimation Errors for Octahedral Crystals When Noise is Added (Averaged Over 1000 Realizations)

		Gamma ($m' = 13$)	Exponential ($m' = 87$)	Bimodal ($m' = 36$)
10 s	$\|\boldsymbol{v}\|_2$	8.82×10^{-4}	8.82×10^{-4}	8.82×10^{-4}
	$\boldsymbol{UB}(m')$	4.25×10^{-4}	162	0.0308
	$\|\boldsymbol{e}_1\|_2$	6.04×10^{-5}	4.46×10^{-4}	8.79×10^{-5}
	$\|\boldsymbol{e}_2\|_2$	2.04×10^{-5}	0.0185	5.70×10^{-4}
	e_{rel}	8.13×10^{-3}	0.319	0.0557
20 s	$\|\boldsymbol{v}\|_2$	4.44×10^{-4}	4.44×10^{-4}	4.44×10^{-4}
	$\boldsymbol{UB}(m')$	2.14×10^{-4}	81.4	0.0155
	$\|\boldsymbol{e}_1\|_2$	6.04×10^{-5}	4.46×10^{-4}	8.79×10^{-5}
	$\|\boldsymbol{e}_2\|_2$	9.78×10^{-6}	9.21×10^{-3}	2.93×10^{-4}
	e_{rel}	7.69×10^{-3}	0.159	0.0297
30 s	$\|\boldsymbol{v}\|_2$	2.17×10^{-4}	2.17×10^{-4}	2.17×10^{-4}
	$\boldsymbol{UB}(m')$	1.04×10^{-4}	39.8	7.57×10^{-3}
	$\|\boldsymbol{e}_1\|_2$	6.04×10^{-5}	4.46×10^{-4}	8.79×10^{-5}
	$\|\boldsymbol{e}_2\|_2$	4.71×10^{-6}	4.70×10^{-3}	1.43×10^{-4}
	e_{rel}	7.58×10^{-3}	0.0813	0.0164

The cutoff value of m' used here is the one previously used for the noise-free case.

reconstruction error. Table 2 shows that this is satisfied for the gamma distribution, and thus $e_{\text{rel}} < 1\%$ for all three noise levels. However, at the highest noise level (10 s sampling), notice that $\boldsymbol{e}_2$ is becoming significant relative to $\boldsymbol{e}_1$.

Figure 11 illustrates the tradeoffs between $\boldsymbol{e}_1$ and $\boldsymbol{e}_2$ for the octahedral crystal and the gamma distribution. The results are shown here for the 10 and 30 s sampling. The values of $\|\boldsymbol{e}_2\|_2$ that are plotted are the averages over 1000 realization of the noise, whereas the upper bound UB is a bound on any single realization. At the highest noise level of 10 s, this bound gives a value of $m' = 9$, whereas at the lower noise level of 30 s, $m' = 12$. Since in the noise-free case $m' = 13$, according to our analysis procedure m' should be between 9 and 13 for 10 s sampling, whereas for 30 s sampling, m' could be 12 or 13. Thus, this upper bound on $\boldsymbol{e}_2$ appears to be useful in guiding the selection of m' in the presence of measurement noise, at least for the gamma distribution.

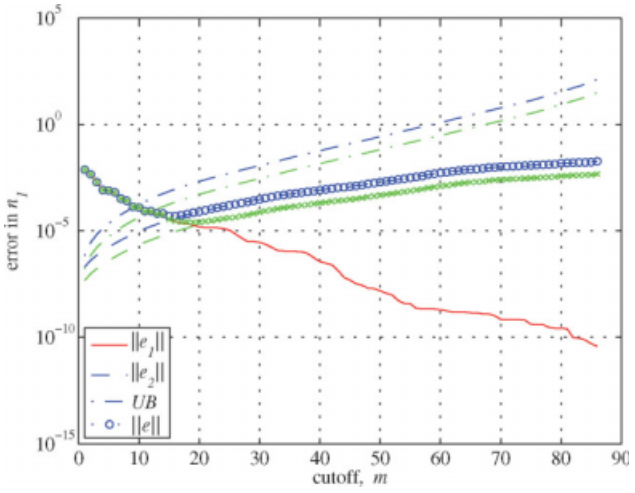

Figure 11. Comparison of the reconstruction error for the octahedral shape and the gamma distribution, for varying cutoff m'.

The dark (blue) curves are for 10 s sampling, and the light (green) curves are for 30 s sampling. The norm of the total error $\boldsymbol{e}$ is plotted using symbols ('o' for 10 s, 'x' for 30 s). The component errors due to truncation ($\boldsymbol{e}_1$) are plotted with a solid (red) line, whereas the portions due to noise ($\boldsymbol{e}_2$) are plotted with a dashed line. The upper bound UB on $\boldsymbol{e}_2$ is denoted with the dash-dot line. [Color figure can be viewed in the online issue, which is available at www.interscience.wiley.com.]

When the exponential distribution is considered, the measurement noise has a more significant effect on the reconstruction of $\boldsymbol{n}_1$, due to the large number of eigenvectors retained ($m' = 87$). In Figure 12, this error is most evident below 100 μm and for the 10 s sampling. In Table 2, we see that the overall error is 32% for the 10 s sampling and 8% for the 30 s sampling. Recall that in the noise-free case, the error was less than 1%. For the case of 10 s sampling, our cutoff criterion gives $m' = 37$, whereas in fact the minimum error of 20% can be calculated at $m' = 70$, which falls between 37 and 87.

The results for the bimodal distribution are also summarized in Table 2. As in the noise-free case, the bimodal distribution is more difficult to estimate than the gamma distribution, but is easier than the exponential distribution. For the nominal value $m' = 36$, $\|\boldsymbol{e}_2\|_2 > \|\boldsymbol{e}_1\|_2$, such the overall reconstruction errors e_{rel} are greater than 1%. For the case of 10 s sampling, the error is 5.6%, whereas a minimum error of $e_{\text{rel}} = 4.7\%$ can be achieved using $m' = 32$. Our upper bound calculation gives $m' = 20$. Again, the optimum lies between the cutoff value given by the bound and the value for the noise-free case.

A comparison between the previously detailed method and the CLSM method described by Ruf et al.[5] is shown for the bimodal distribution in Figure 13. Non-negativity and normalization constraints are applied, and the smoothening parameter is selected using the criterion in Ref. 5. The CLSM method smoothens out most of the noise at low sizes L, but therefore cannot fully capture the sharp peak at 200 μm. In contrast, our method (using $m' = 30$) does not have this inherent tradeoff and may perform better at restoring sharp features of the population density, which are smoothed out

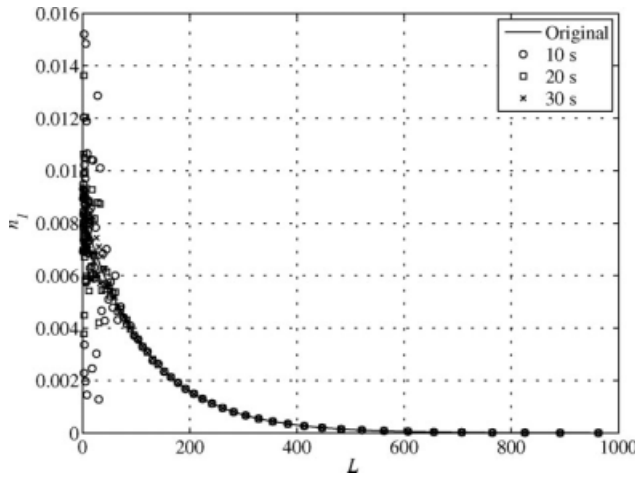

Figure 12. Restoration of the exponential population density from a noisy chord-length histogram, using $m' = 87$.

The crystal shape is octahedral.

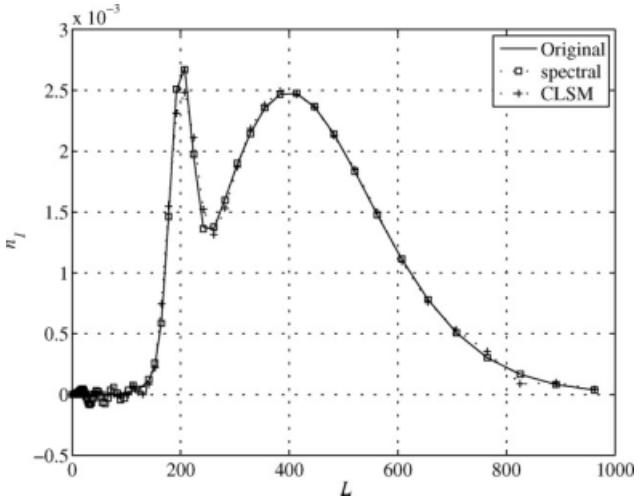

Figure 13. Comparison of the spectral method to CLSM, for a noise based on a measurement every 10 s, for a bimodal distribution and octahedral crystal shape.

by the CLSM. In practice, the best approach may be to combine our approach with additional smoothing, when deemed appropriate (i.e., exponential distributions).

Conclusions

The FBRM is a commonly used tool in monitoring the progression of chord-length measurements in batch crystallization. The methodology demonstrated here offers an accurate, constraint-free estimation of the population density from the chord length distribution. The spectral method can be efficiently applied to a wide range of nonspherical particle shapes, as well as multimodal and sharp population density functions.

The principal component analysis offers a straightforward alternative to restore the population density from chord-length data, and it requires little computation. It also provides an analysis of which aspects of the population density can accurately be restored. The size of the observable subspace is a function of the crystal geometry and the precision desired. Note that as the geometry becomes more elongated, a drop in the singular values is seen which defines the limits of the accuracy of the recovery process, as it sets a limit to the size of both observable and nonobservable subspace and the accuracy of the recovery. As the needles get thinner, the size of the unobservable subspace increases and the restoration of the population density for the lower size ranges are more challenging. The accuracy of the proposed method is therefore limited by the geometry of the considered population. The projections onto the observable and unobservable subspaces tend to be highly oscillatory in small sizes range. Those features are more difficult to estimate because all crystal sizes contribute to small chords whereas only larger ones create large chords. Note that extreme oscillations can occur in the smaller bins sizes during the restoration and also that the smaller bins are more sensitive to noise, thus making it harder to effectively estimate those populations, especially for the exponential distribution. A smoothing can still be applied later to the restored density if needed.

Estimation is limited by the noise in measurements of the chord-length data, which can be reduced by increasing the data acquisition time frame. The data presented here shows that 10 s sampling is sufficient for the gamma distribution, but that time frames above 30 s may be needed for exponential and bimodal distributions. Also, it was shown that, when compared with CLSM, the spectral method may provide a better restoration of population densities with sharp features. Although our method provides an alternative method for estimating population density, its greater contribution may be for the analysis and error bounds; specifically, the analysis can help tailor the FBRM settings of number of bins, size distribution of bins, and integration time, for the particular crystal shape and distribution function appropriate to a particular process. Furthermore, the presented methodology has the potential to be the basis for a control scheme that manipulates the population density based on the FBRM.

Notation

A = symmetric matrix
b = vector
CLD = chord-length density
C = proportionality constant in the upper bound UB on $\boldsymbol{e}_2$
e = error vector for $\boldsymbol{n}_1$
e_1 = error vector in $\boldsymbol{n}_1$ due to projection
e_2 = error vector in $\boldsymbol{n}_1$ due to measurement noise
e_{rel} = relative error in $\boldsymbol{e}$
FBRM = focused beam reflectance measurement
k = chord-length histogram
k_{est} = estimated chord-length histogram
L = crystal characteristic size
m = number of eigenvectors
m' = number of vector defining the observable subspace
$m'_{\max}$ = maximum number of vector defining the observable subspace
$\boldsymbol{n}_1$ = normalized length-weighted population density
$\boldsymbol{n}_{1,\text{obs}}$ = projection of $\boldsymbol{n}_1$ onto the observable subspace
$\boldsymbol{n}_{1,\text{unobs}}$ = projection of $\boldsymbol{n}_1$ onto the unobservable subspace
$\boldsymbol{n}_{1,\text{est}}$ = estimated length-weighted population density
N_{b} = number of bins
q = normalized chord-length density
PAT = Process Analytical Technology
UB = upper bound on the $\boldsymbol{n}_1$ error due to measurement noise
U = orthonormal eigenvector of $\boldsymbol{A}$
$\boldsymbol{u}_{\text{i}}$ = eigenvectors of $\boldsymbol{A}$, basis vectors of $\boldsymbol{U}$
$\boldsymbol{v}$ = measurement noise vector
s = chord length
α_i = projection coefficient for the population density
β = shape factor for the gamma function
ε_{tol} = tolerance on project error for $\boldsymbol{n}_1$
γ = normalizing coefficient for the gamma function
ΔN = number size population density
θ = scale parameter for the gamma function
λ_i = eigenvalues of $\boldsymbol{A}$
σ_i = singular values of Ψ
Ψ = conversion matrix
ω = standard deviation vector for zero-mean normally distribution measurement noise

Literature Cited

1. Barthe S, Rousseau RW. Utilization of focused beam reflectance measurement in the control of crystal size distribution in a batch cooled crystallizer. *Chem Eng Technol*. 2006;29:206–211.
2. Yu W, Erickson K. Chord length characterization using focused beam reflectance measurement probe—methodologies and pitfalls. *Powder Technol*. 2008;185:24–30.

3. Li M, Wilkinson D. Determination of nonspherical particle size distribution from chord length measurements. *Theor Anal Chem Eng Sci*. 2005;60:3251–3265.
4. Li M, Wilkinson D, Patchigolla K. Determination of non-spherical particle size distribution from chord length measurements. Part II: Experimental Validation. *Chem Eng Sci*. 2005;60:4992–5003.
5. Ruf A, Worlitschek J, Mazzotti M. Modeling and experimental analysis of PSD measurement through FBRM. *Part Part Syst Charact*. 2000;17:167–179.
6. Worlitschek J, Hocker T, Mazzotti M. Restoration of PSD from chord length distribution data using the method of projections onto convex sets. *Part Part Syst Charact*. 2005;22:81–98.
7. Worlitschek J, Mazzotti M. Model-based optimization of particle size distribution in batch cooling crystallization of paracetamol. *Cryst Growth Des*. 2004;4:891–903.
8. Wynn EJW. Relationship between particle-size and chord-length distributions in focused beam reflectance measurement: stability of direct inversion and weighting. *Powder Technol*. 2003;133:125–133.
9. Nagy ZK, Fujiwara M, Woo XY, Braatz RD. Determination of the kinetic parameters for the crystallization of paracetamol from water using metastable zone width experiments. *Ind Eng Chem Res*. 2008;47:1245–1252.
10. Kail N, Briesen H, Marquardt W. Analysis of FBRM measurements by means of a 3D optical model. *Powder Technol*. 2008;185:211–222.
11. Barthe SC, Grover MA, Rousseau RW. Observation of polymorphic change through analysis of FBRM data: transformation of paracetamol from Form I to Form II. *Cryst Growth Des*. 2008;8:3316–3322.
12. Beers K. *Numerical Methods for Chemical Engineering*. Cambridge, U.K.: Cambridge University Press, 2007.
13. Jackson D. Stopping rules in principal component analysis: a comparison of heuristical and statistical approaches. *Ecology*. 1993;74:2204–2214.
14. Cangelosi R, Goriely A. Component retention in principal component analysis with application to cDNA microarray data. *Biol Direct*. 2007;2:2.
15. Jolliffe IT. *Principal Component Analysis*. Berlin: Springer-Verlag, 2002.
16. Frontier S. Etude de la décroissance des valeurs propres dans une analyse en composantes principales: comparaison avec le modèle du bâton brisé. *J Exp Mar Biol Ecol*. 1976;25:67–75.
17. Vargas-Ubera J, Aguilar J, Gale D. Reconstruction of particle-size distributions from light-scattering patterns using three inversion methods. *Appl Opt*. 2007;46:124–132.

Appendix

Begin with the relationship

$$\boldsymbol{b} = \boldsymbol{A}\boldsymbol{x} \tag{A1}$$

where $\boldsymbol{A}$ is a real symmetric matrix such that $\boldsymbol{A} = \Psi^{\mathbf{T}}\,\Psi$, $\boldsymbol{b}$ is a known vector and $\boldsymbol{x}$ is an unknown vector. The eigenvalues of $\boldsymbol{A}$, $\lambda_i = {\sigma_i}^2$, and the eigenvectors $\boldsymbol{u}_i$ have been computed. σ_i are defined to be the singular values of the matrix Ψ. An orthonormal basis $\boldsymbol{U}$ can be defined using the eigenvectors. It is then possible to describe any real vector $\boldsymbol{b}$ by its projection onto this basis according to the following equation:

$$\boldsymbol{b} = \sum_{i=1}^{m} \frac{(\boldsymbol{u}_i \cdot \boldsymbol{b})}{(\boldsymbol{u}_i \cdot \boldsymbol{u}_i)} \boldsymbol{u}_i = \sum_{i=1}^{m} (\boldsymbol{u}_i \cdot \boldsymbol{b}) \boldsymbol{u}_i \tag{A2}$$

Because the basis is normal, $\boldsymbol{u_i} \cdot \boldsymbol{u_i} = 1$. To solve Eq. A1, we express $\boldsymbol{x}$ in terms of the basis $\boldsymbol{U}$, with the α_i defined as real but unknown scalar coefficients.

$$\boldsymbol{x} = \sum_{i=1}^{m} \alpha_i \boldsymbol{u_i} \tag{A3}$$

Therefore, since $\boldsymbol{A}$ is a linear operator, Eq. A1 becomes

$$\sum_{i=1}^{m} \alpha_i \boldsymbol{A}\boldsymbol{u_i} = \sum_{i=1}^{m} (\boldsymbol{u_i} \cdot \boldsymbol{b}) \boldsymbol{u_i} \tag{A4}$$

Since $\lambda_{\mathrm{i}} = {\sigma_{\mathrm{i}}}^2$ and $\boldsymbol{u}_i$ are, respectively, the eigenvalues and eigenvectors associated with $\boldsymbol{A}$,

$$\boldsymbol{A}\boldsymbol{u_i} = \lambda_i \boldsymbol{u_i} = \sigma_i^2 \boldsymbol{u_i} \tag{A5}$$

Equation A4 can be simplified to

$$\sum_{i=1}^{m} \alpha_i \sigma_i^2 \boldsymbol{u_i} = \sum_{i=1}^{m} (\boldsymbol{u_i} \cdot \boldsymbol{b}) \boldsymbol{u_i} \tag{A6}$$

Therefore,

$$\alpha_i = \frac{(\boldsymbol{u_i} \cdot \boldsymbol{b})}{\sigma_i^2}, \quad i = 1, ..m \tag{A7}$$

The vector $\boldsymbol{x}$ can then be estimated according to:

$$\boldsymbol{x} = \sum_{i=1}^{m} \left(\frac{(\boldsymbol{u_i} \cdot \boldsymbol{b})}{\sigma_i^2} \right) \boldsymbol{u_i} \tag{A8}$$

Manuscript received Mar. 28, 2008, and revision received Jan. 22, 2009.